Angular Irradiation Methods for DOI Calibration of Light-Sharing Detectors—A Perspective for PET In-System Calibration

Yannick Kuhl, *Graduate Student Member, IEEE*, Stephan Naunheim, *Graduate Student Member, IEEE*, David Schug, Volkmar Schulz, *Senior Member, IEEE*, and Florian Mueller, *Graduate Student Member, IEEE*

***Abstract*—Typical positron emission tomography (PET) detectors consist of one-layer segmented scintillators coupled to silicon photomultipliers (SiPMs). Light-sharing detectors, e.g., semi-monoliths, additionally provide depth-of-interaction (DOI) estimation, performing best when calibrated individually. To establish those designs in large PET systems, scalable (re-)calibration methods are needed, possibly transferable to assembled systems. Here, two DOI calibration methods, potentially allowing in-system calibration, are evaluated and compared with an established calibration scheme. Both methods are based on angular detector irradiation using a fan-beam slit collimator and gradient tree boosting (GTB) for 3-D position estimation. The positioning performance was assessed for irradiation angles between 0° (lateral) and 90° (detector normal). With lateral irradiation, a unique DOI position is given, whereas with angular irradiation a gamma-individual reference position must be retrieved. The first method employs one angular beam and calculates DOI from the beam path and planar position estimation. The second method uses two intersecting beams. The intersection defines DOI for gamma interactions that are spatially localized there. Those gamma photons are identified by light distribution comparison using a *k*-nearest neighbor routine. The methods were evaluated on a semi-monolithic LYSO slab detector (32 × 3.9× 19 mm^3 slabs). Both methods performed similarly to the benchmark lateral irradiation within 1% and 6%, respectively, for shallow irradiation angles up to 45°.**

***Index Terms*—Angular beam irradiation, PET detector calibration, depth-of-interaction (DOI), fan-beam collimator, in-system calibration, (semi-)monolithic scintillator.**

Manuscript received 10 March 2023; accepted 10 April 2023. Date of publication 15 May 2023; date of current version 4 September 2023. This work was supported by the Federal Ministry of Education and Research (BMBF) under Contract 13GW0621B. *(Volkmar Schulz and Florian Mueller are co-last authors.) (Corresponding authors: Yannick Kuhl; Volkmar Schulz)*

This work did not involve human subjects or animals in its research.

Yannick Kuhl, Stephan Naunheim, and Florian Mueller are with the Department of Physics of Molecular Imaging Systems, Institute for Experimental Molecular Imaging, RWTH Aachen University, 52074 Aachen, Germany (e-mail: yannick.kuhl@pmi.rwth-aachen.de; volkmar.schulz@pmi.rwth-aachen.de).

David Schug is with the Department of Physics of Molecular Imaging Systems, Institute for Experimental Molecular Imaging, RWTH Aachen University, 52074 Aachen, Germany, and also with the Hyperion Hybrid Imaging Systems GmbH, 52074 Aachen, Germany.

Volkmar Schulz is with the Department of Physics of Molecular Imaging Systems, Institute for Experimental Molecular Imaging, and the Physics Institute III B, RWTH Aachen University, 52074 Aachen, Germany, and also with the Hyperion Hybrid Imaging Systems GmbH, 52074 Aachen, Germany.

Color versions of one or more figures in this article are available at https://doi.org/10.1109/TRPMS.2023.3272015.

Digital Object Identifier 10.1109/TRPMS.2023.3272015

I. Introduction

POSITRON emission tomography (PET) is a noninvasive functional imaging technique with proven clinical and preclinical value [1], [2], [3]. In an arrangement of radiation detectors, gamma photon pairs of 511-keV energy each are detected in a conversion process, starting with a conversion to a large number of optical photons in a scintillator (i.e., LSO, LYSO, and BGO). A photodetector, typically consisting of several readout channels with outer dimensions of a few millimeters, further converts the optical photons to a measurable electric signal [4].

In current PET systems, typically one-layered pixelated scintillator arrays are used with thicknesses of about (15 to 30) mm [5]. These designs achieve good energy and time resolution while they are limited in spatial resolution (SR) by their planar crystal dimensions with typical sizes of (3 to 4) mm [6], [7]. In addition, such arrays do not provide the possibility to encode depth of interaction (DOI) information. The resulting parallax errors (radial astigmatism) deteriorate the SR. This effect particularly affects small-diameter PET systems, such as small-animal scanners or organ-dedicated scanners, for off-centered interactions (transverse resolution) [8], [9] and total-body PET systems with a long axial field of view (axial resolution) [10].

Researchers are investigating various detector concepts that enable DOI encoding [11]. These include multilayer designs with multiple shifted pixelated layers [12], double-sided readout [13], [14], [15], [16], [17], light-sharing between selected scintillator elements [18], [19], combinations of scintillators with different physical properties (e.g., phoswich detectors [20]), and subsurface laser engraving [21]. However, these approaches often involve higher complexity or higher costs but generally do not require a dedicated calibration setup using, e.g., collimators. Light-sharing detectors (e.g., monolithic scintillators [22], [23], [24], [25], [26], [27], [28]) with light distributions over multiple readout channels are another widely used design at a comparable cost to one-layer pixelated arrays. Such designs intrinsically offer DOI capability due to individual light distributions depending on the planar and DOI gamma interaction position.

In this work, light-sharing semi-monolithic slab scintillators are used, which spread the optical photons mainly along one monolithic dimension. Thus, they keep the intrinsic

DOI-encoding capabilities of monoliths while constraining the optical photons to a reduced readout area [25], [26], [29], [30], [31]. Using positioning methods, the gamma interaction position can be estimated from the light distribution. It can be distinguished between parametric methods (e.g., first moment [32], nonlinear least-square modeling [33], Cauchy modeling [34], and local linear embedding [35]) and statistical methods (*k*-nearest neighbors [36], maximum likelihood [37], [38], neuronal networks [39], Voronoi diagrams [40], and gradient tree boosting (GTB) [25], [26]). Statistical methods show overall superior performance compared to parametric approaches, especially toward the detector edges, by correcting for nonuniformities in the detector response through a calibration process [40]. Nonuniformities can be, for example, the absence of adjacent readout channels at the edges, optical defects in the scintillator material, or irregularities in the interface between the scintillator and photodetector.

However, the calibration process is currently a time-consuming and labor-intensive procedure. A complete detector calibration lasts days to weeks with common calibration routines, such as the parallel hole beam collimator [41]. Extended setups with multiple holes accelerate this process [42]. Further acceleration while simplifying the design can be achieved with fan-beam-based setups, especially for DOI calibration, currently down to hours per detector [26], [36], [43]. Yet, in large PET systems with possibly several hundred detectors, a full system calibration would scale accordingly and is thus costly. Similarly, scaled setups could speed up the initial calibration process, but the detectors would have to be removed from the PET system again for recalibration. Detector recalibration may be necessary, for example, due to changes in the operating point (e.g., the bias voltage of the silicon photomultipliers (SiPMs), temperature), or due to individual, age-related changes in the detector properties, such as the optical interfaces between crystals, sensor, and, e.g., reflective foils. In-system calibration addresses both problems by scaling the calibration process directly in the system to multiple detectors at once reducing the system calibration time to possibly hours for an entire detector ring.

Current planar calibration methods are methodologically suitable for in-system calibration and could be implemented via suitable (multi-)fan-beam collimator designs [44], [45], or electronic point-source collimation [46]. However, current DOI calibration routines with the most attractive positioning performance are based on lateral detector irradiation [26], [47] which is not feasible in an assembled detector ring. A time-consuming and labor-intensive disassembly and reassembly with long scanner downtimes would be required. During this process with mechanical effects on the detectors, their properties could change, which would negatively influence the positioning model quality, or the detectors could even get damaged in the worst case. One approach to simplify the process is to create cross-detector positioning models [39], [42]. The approach chosen in this work, however, retains the detector-individual calibration by replacing lateral irradiation with angular detector irradiation to potentially enable in-system calibration such as shown in Fig. 1. Since the known reference

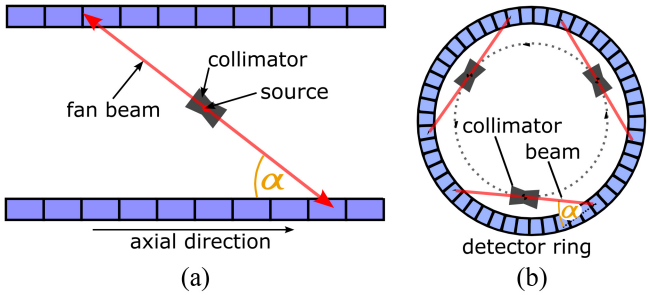

Fig. 1. DOI in-system calibration variants. (a) Angular detector irradiation along the axial direction. (b) Detector irradiation along the radial direction. The collimator is stepped in the respective direction to cover multiple positions per detector. The axial design could have a cone-shaped collimator for simultaneous detector irradiation in the radial direction.

irradiation position is lost in the process, a methodology is needed to determine this reference DOI position for each gamma photon from the angular irradiation. A rough DOI for the individual gamma interactions can be calculated, for example, from a previous planar position estimation and the known beam path [38], [48]. Further theoretical concepts and simulation studies in [49], [50], and [51] showed that a recovery of the DOI reference position from two gamma beams intersecting in the scintillator volume may be possible.

This work introduces and experimentally assesses two angular DOI calibration routines combined with a machine learning-based gamma position estimation. The concept of those angular calibration routines is transferable to any detector design with changing light distributions depending on the gamma interaction position. The first mono-angle method is based on angular detector irradiation using one fan beam. The second dual-angle method utilizes two intersecting fan beams in the crystal volume. We present a detailed experimental analysis of the angular dependence of both routines not found in the current literature, answering fundamental questions for in-system (re-)calibration of (semi-)monolithic detector designs.

II. Materials

A. Radiation Detector

In this work, the main components of the radiation detector consist of eight semi-monolithic scintillator slabs coupled to a DPC3200-22-44 sensor tile [philips digital photon counting (PDPC)] Fig. 2(b) as described in the following Section II-A2). The PDPC technology evaluation kit (TEK) was utilized as the readout architecture. Conceptually, the developed calibration procedures are transferable to analog readouts and digitalization schemes, as well as to other scintillator geometries.

1) Photosensor: A detailed description of the sensor tile can be found in [52] and [53]. An array of 4×4 digital SiPMs, the DPC3200-22 (DPC), forms the sensor tile with an area of 32.6 × 32.6 mm^2. Every DPC in turn consists of an array of 2 × 2 readout channels, each containing 3200 single-photon avalanche diodes (SPADs). One DPC returns four-photon count values corresponding to the readout channels and a timestamp, called "hit," that is passed to the

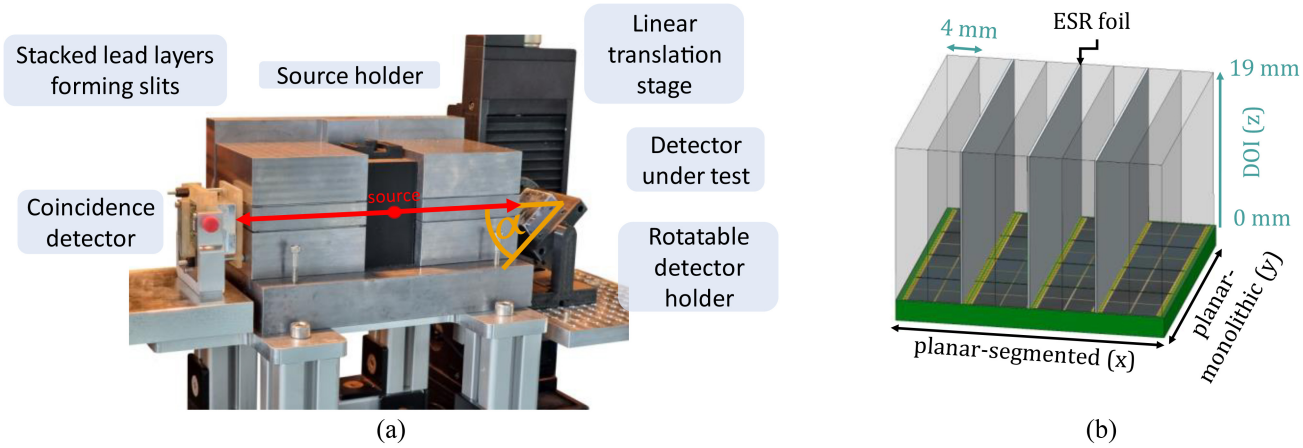

Fig. 2. (a) Fan-beam collimator setup. The collimator consists of lead layers stacked with thin feeler gauge stripes to create the slits for the gamma beam. The radioactive sources are housed in a modular source holder in the center of the setup. Surrounding lead shieldings offer radiation protection. The double-sided irradiation enables the addition of a coincidence detector. The detector under test is movably placed on a linear translation stage for the calibration procedure. (b) Schematic depiction of the semi-monolithic slab detector design. Each LYSO slab covers one readout channel column of the DPC3200-22-44 sensor tile. Every pair of slabs is separated by ESR foil, which additionally surrounds the scintillator on the outside.

readout architecture. Each DPC is self-triggering and due to trigger probabilities and possible dead times, gamma interactions at the same position in the scintillator can have a different set of DPCs to trigger, validate and send out data. Using slab detectors as an example, a gamma photon interaction may have resulted in all DPCs to be read out under the slab of interaction, while another gamma photon interaction at the same interaction position has a missing DPC readout resulting in incomplete data.

2) Slab Scintillator Configuration: We investigated a set of eight LYSO scintillator slabs (Crystal Photonics, Sanford, FL, USA) of dimensions $31.9 \times 3.9 \times 19$ mm^3, coupled to the sensor tile via Meltmount (Cargille Laboratories, Cedar Grove, NJ, USA) with each slab covering one readout channel column (see Fig. 2). Thus, the used slabs are a combination of the one-to-one coupled and the monolithic designs, offering intrinsic DOI information like monoliths but with a higher optical photon density. Every pair of slabs is separated by reflective foil (ESR, 3M, Maplewood, MN, USA) to reduce light-sharing and additional ESR foil wrapping on all outer surfaces of the crystals to further confine the optical photons to the scintillator medium. A detailed analysis of this specific detector configuration can be found in a recent work [27].

B. Calibration Setup

The detector calibration is performed by means of a fan-beam collimator enabling a time-efficient calibration process. The collimator design is based on the modular multifan-beam collimator presented in [44]. Two positron-emitting ^{22}Na point sources with a total of $\sim$20 MBq activity were placed centrally in the collimator. The gamma photon flux from the sources is confined in its solid angle by one slit between stacked lead plates to create a gamma fan beam that irradiates two opposing, identical slab detectors in a coincidence setup (Fig. 2). The detector under test was fixed on a linear translation stage (LIMES 90, Owis, Staufen im Breisgau, Germany) with a nominal maximum positioning error of 2 μm. The setup was placed in a light-tight climatic cabinet with an ambient temperature of 10 °C at 30%–40% humidity.

The collimator slit in the direction of the detector under test was set to 0.5 mm, while the slit in the direction of the coincidence detector was set to 1 mm with the coincidence detector placed closer to the radioactive sources to avoid gamma photon losses due to geometric effects and fabrication inaccuracies in the setup. Using a coincidence count rate measurement according to [41], a beam profile was obtained showing a full-width half maximum (FWHM) of 0.48 mm for the 0.5-mm slit width directly at the collimator and an FWHM of 0.57 mm at a detector-to-slit distance of about 25 mm. The dataset for this analysis comprised three million events collected in a range of 8 mm around the edge with a stepping pitch of 0.1 mm and 120-s measurement time per position. Effectively, a much smaller dataset would be sufficient for the analysis by at least a factor of 10. The detector under test was fixed on a rotatable holder for angular irradiation (Fig. 2). Depending on the angle set, distances of 20–25 mm between the collimator and the closest detector edge resulted.

III. Methods

In the following, the general position estimation routine is described, which is valid for both the planar and the DOI calibration. A planar calibration was performed in advance as an available parameter for the DOI calibration routines. Subsequently, the developed angular irradiation methods are introduced that are based on this position estimation routine.

The sensor tile was operated at a temperature of 13 °C–15 °C at 25.2-V bias voltage with an overvoltage of 2.6 V and 10% inhibit fraction. Trigger scheme 3 was utilized requiring on average 3.0 ± 1.4 cell discharges on one readout channel to trigger [52], [54]. Validation scheme 4 was chosen corresponding to an average of 17.0 ± 6.2 cell discharges that are required on a readout channel. The validation length was set to 10 ns.

A. Calibration Data Acquisition

The aim of the calibration data acquisition is to collect gamma photon interactions at different known positions over

the detector volume for the subsequent positioning model training. Therefore, the detector was stepped through the fan beam in a grid of 0.25-mm steps, for all measurements, along the monolithic directions using the linear translation stage. For planar-monolithic calibration, the fan beam was incident in the direction of the detector normal ($\alpha = 90°$) while irradiating all slabs. For DOI calibration with lateral irradiation, the fan beam and photosensor surface are parallel to each other ($\alpha = 0°$) with the irradiation direction along the slabs. The angular irradiation methods have irradiation angles between the described planar and DOI alignment corresponding to $\alpha = \{11.25°, 22.5°, 33.75°, 45°, 56.25°, 67.5°, 78.75°\}$. The measurement time per position was set to 45 s for the DOI measurements. For all routines, at maximum one-third of the acquired data was considered for the analysis. This resulted in an effective calibration time of about 17 min for the lateral irradiation method. For the angular methods the calibration time changes due to the changing projection of the crystal to be irradiated and the constant grid pitch of 0.25 mm. Thus, the effective calibration time increased for the mono-angle method from 18 min for $\alpha = 11.25°$ to up to 33 min for $\alpha = 56.25°$ with double the calibration time for the dual-angle method. With calibration data optimized angular routines as well as using dedicated in-system setups we expect the system calibration time to be lowered by several factors to a full system calibration within a few hours. Corresponding scaled fan-beam collimators can have multiple slits for simultaneous irradiation of several detector ring segments such as illustrated in [45].

B. General Gamma Photon Positioning Routine

The general position estimation in planar-monolithic and DOI direction Fig. 2(b) follows the scheme of preprocessing steps of the acquired calibration data and the creation of a positioning model. Based on this positioning model, a position estimation for new gamma interactions is obtained. For the planar-segmented direction, the gamma interaction position is given by the corresponding slab of interaction resulting from the pixel with the highest optical photon count value (main pixel). An alternative assignment could be based on the highest photon sum below the slabs. Both methods gave the same result in about 98% of the cases. The assignment differs in over 70% of cases by one slab position, mainly caused by a missing DPC readout. We decided to use the main pixel-based method, to remain consistent with previous work.

1) Data Preprocessing: In preprocessing according to [32], the individual "hits" that are within 40 ns, are correlated to one gamma interaction to form a so-called cluster. Then a coincident counterpart was searched for within a time window of 10 ns, resulting in a pair of events. Only events with an optical photon count sum in the range of 400–3000 were considered to filter events in a distant region from the uncalibrated photopeak at about 2150 optical photons. This photon filter was applied to all measurements. A more specific energy filter constrains the calculated gamma energies (Section III-G) in a clinical energy window of (435 to 585) keV for part of the evaluations.

For lateral irradiation, the number of events along the incident planar-monolithic direction follows an exponential intensity decay. A bias effect in the machine learning algorithm (see below) along the planar-monolithic direction would thus occur [25], [26]. Therefore, the number of events per irradiation position was normalized along the planar-monolithic direction with the planar position information estimated using the prior planar-monolithic calibration. Additionally, the number of events per irradiation position was normalized to 10 000, 2500, and 2500 for training, validation, and test dataset, respectively, to further mitigate bias effects along DOI.

To normalize the number of events with the angular irradiation-based methods, the crystal was divided into equally sized voxels over the detector volume. Using the planar position information, as well as the calculated DOI, the events were filled into those voxels and the events per voxel were normalized. The voxels covered one readout channel in the planar-segmented direction and separate the planar-monolithic direction into 32 and the DOI direction into 19 segments, representing a pitch of 1 mm. Using voxels of larger dimension led to an increased bias effect. The number of events per voxel was chosen to $\sim$154 to match the dataset size of the lateral irradiation of 750 000 events.

2) Gradient Tree Boosting-Based Position Estimation: For gamma position estimation the supervised machine learning technique GTB was used. We chose the already established algorithm due to generally good positioning performance as shown in previous work [25], [26], [55]. Furthermore, GTB was demonstrated for high-throughput implementations in both CPU [55] and FPGA [56]. GTB is a supervised machine learning technique based on sequential binary decision trees. In an additive training procedure, a positioning model is trained starting in the first tree with the known irradiation position. The following trees use residuals between irradiation position and estimation of the already established ensemble. Each tree aims to minimize the errors of the previous tree with the root mean squared error (RMSE) (see below) as the loss function. The final position estimation equals the sum of all leaves.

The algorithm can be tuned via hyperparameters. In this work, four are of particular importance which led to good results in previous work.

1) *Number of Decision Trees:* Trees are added to the ensemble until the RMSE did not improve for ten consecutive rounds with a maximum of 1000.
2) *Maximum Depth:* The maximum number of binary decisions per decision tree (planar: 10, DOI: 12).
3) *Learning Rate:* Denotes how fast the model learns by multiplying the learning rate with the residual of the established ensemble (planar: 0.1, DOI: 0.1).
4) *Input Features:* GTB handles arbitrary input features. In this work the following features were used for the DOI training: unnormalized pixel photon counts of all pixels of the triggered DPCs of a cluster, first and second moment of all raw optical photon values per cluster, main pixel (readout channel with the highest optical photon count), main DPC (DPC containing the main pixel), column photon sum, row photon sum, total photon sum, squared pixel intensities on the main DPC (SPIMD).

The positioning models are created based on a training and a test dataset, both with known reference irradiation position. Another validation dataset is used for the dual-angle method to tune the method's hyperparameters. This tuning was performed once for $\alpha = 45°$. Both the validation dataset and test dataset for the DOI positioning performance evaluations are obtained from the lateral irradiation method (see below) and consist of 2500 events per beam position.

3) Positioning Performance Evaluation: The comparison between gamma position estimations (y_i, z_i) and the fan-beam irradiation position (Y, planar-monolithic; Z, DOI) yields various positioning performance parameters. The histogram of all position estimation errors ($z_i - Z$) represents the point-spread function (PSF) with the FWHM defined as the SR. We determined the SR with a fitting routine based on the NEMA NU 4-2008 procedure for PET scanner performance characterization [57]. Based on those position estimation errors, further performance parameters can be defined, such as the mean absolute error (MAE) (1), bias vector (Bias) (2), the RMSE (3), and the percentile radius 50, 90 (r_{50}, r_{90}). The parameters can be calculated for each lateral irradiation position Z individually, or globally as the mean of the local parameters over all irradiation positions.

A statistical error on the MAE and SR performance parameters was estimated using the available datasets. For this purpose, the resulting PSF was divided into ten subsets and the MAE was determined again for each subset. The error on the mean value was less than 0.01 mm in agreement with previous estimates. The uncertainty on the SR was less than 0.04 mm

$$\mathrm{MAE}(Z) = \frac{1}{\#\gamma}\sum_{i}^{\#\gamma}|z_i - Z| \tag{1}$$

$$\mathrm{Bias}(Z) = \frac{1}{\#\gamma}\sum_{i}^{\#\gamma}(z_i - Z) \tag{2}$$

$$\mathrm{RMSE}(Z) = \sqrt{\frac{1}{\#\gamma}\sum_{i}^{\#\gamma}(z_i - Z)^2} \tag{3}$$

C. Lateral Irradiation Calibration Routine

In this lateral irradiation routine, the detector is irradiated laterally from one direction with the fan-beam parallel to the sensor tile surface (0°). This allows an unambiguous referencing of gamma interaction and DOI position so that this method is considered as the gold standard in this context. Disadvantages of this method can be an increased Compton scatter occurrence due to the long beam path through the scintillator medium with typically larger outer dimensions of the detector compared to the scintillator height. Previous work still showed good results using this method [26]. Another disadvantage resulting from the long beam path in crystal volume is the lower statistics for more distant positions due to the exponential beam intensity decay. This results in increased calibration time or increased effort, for example by irradiating the detector from several sides. Both disadvantages can be reduced with angular irradiation.

D. Single Input Feature Calibration Method

Single input feature-based approaches are capable of DOI estimation via planar detector irradiation, assuming changing DOI measures that are mapped to the DOI gamma interaction probability distribution [58], [59]. Since this method would greatly simplify the in-system calibration process, an estimation of positioning performance will be given here. Applied to monolithic detectors, good results could be obtained with DOI-dependent parameters based on the light distributions, such as "squared pixel intensities divided by the main DPC photon sum" (SPIMD) or "main pixel photon count divided by the main DPC photon sum" (MPBMD) [25], [58] with the main DPC referring to the DPC containing the highest pixel photon count.

In this work, the input features SPIMD and MPBMD are related to a DOI position via lateral irradiation and an isotonic regression (IR) [60] (Fig. 4) by fitting a free-form line. Both features are based on the normalized photon counts of one DPC column below the slab of interaction. Lateral irradiation can be replaced by, e.g., simulating the DOI distribution [58], but is used here as a performance benchmark for this approach.

E. Mono-Angle Calibration Method

In contrast to lateral detector irradiation, the mono-angle method is based on angular fan-beam irradiation for calibration data acquisition with the angle between the fan-beam plane and the sensor tile plane. The DOI position of each event can be determined from the beam path and the prior planar position estimation (Fig. 3) which shows bias effects toward the edges. This simple conversion is physically possible since the refractive index for gamma photons in most materials is approximately 1 [61]. Events that would be assigned a DOI position outside of the crystal volume are discarded. The number of discarded events increases toward steeper irradiation angles with ~3% at $\alpha = 11.25°$ and ~20% at $\alpha = 78.25°$. The DOI position accuracy highly depends on the planar SR as well as the irradiation angle. It is expected that the positioning performance approaches that of the lateral irradiation for smaller angles and collapses for larger angles toward 90°. However, the described occurring scatter effects in the lateral irradiation method could be reduced for steeper irradiation angles.

F. Dual-Angle Calibration Method

The dual-angle method combines two mono-angle irradiations (Fig. 3). For calibration data acquisition in the dual-angle method, the detector is consecutively irradiated with two intersecting beams in the detector volume. The events around this intersection (intersection cluster) can be assigned to the corresponding DOI position (Fig. 3). As a result, this method has little to no dependence on planar positioning performance in contrast to the mono-angle method. Furthermore, by the specific process of determining the intersection clusters, as explained below, Compton scattered gamma interactions may be filtered by the algorithm.

The central task of this method is the determination of the intersection cluster. It is assumed, that similar events

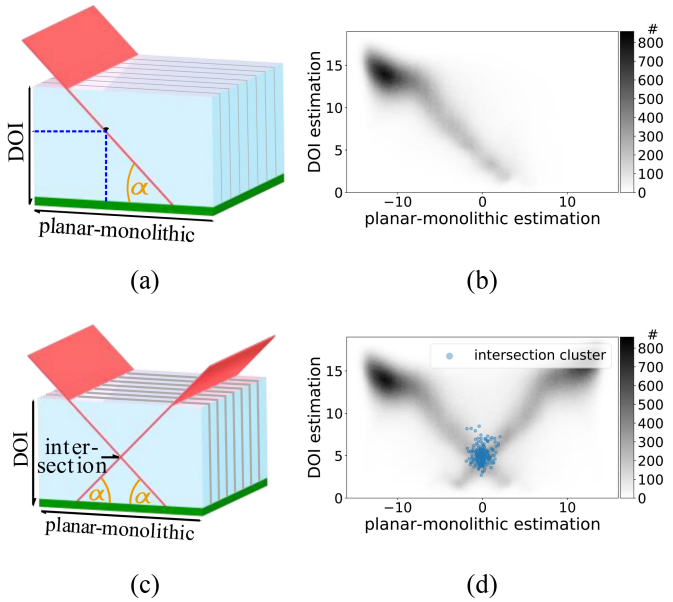

Fig. 3. (a) Schematic mono angular irradiation. The detector stack is irradiated at an angle α with one fan beam (red). The dotted blue line indicates the retrieved DOI position from the planar position estimation. (b) 2-D-histogram of gamma interactions with the estimated DOI position from the lateral irradiation method and the estimated planar position from a planar calibration. This data is only used for illustration. (c) Schematic dual-angle irradiation. Two angular beams (red) intersect in the scintillator volume at a known DOI position from the setup. (d) Beam illustration via a prior planar and DOI position estimation. The white circles represent the selected events (intersection cluster) by the algorithm.

in the photon-count-per-channel space share a similar spatial interaction position in the scintillator volume. Similar events between beam A and beam B can thus be assigned to the intersection cluster. Using a Nearest Neighbors routine [51], [60], the similarity of each event from beam A to the events from beam B and vice versa is calculated. Similarity refers to the distance between the optical photon counts calculated using the Euclidean distance metric

$$d = \sqrt{\sum_{i=1}^{8} \left(p_{A,i} - p_{B,i}\right)^2} \tag{4}$$

with p_A and p_B being the photon counts on the respective readout channels and d the resulting distance. Other Minkowski metrics were tested to lead to similar results and are not further discussed here. This calculation was performed individually per slab to obtain events all over the segmented direction of the detector stack. For processing and positioning performance improvements, only the eight optical photon counts of the pixels below the respective slab of interaction were considered for the routine, with the individual pixel counts normalized by the sum of all the eight-pixel counts. Additional features to the optical photon counts, including the first moment, photon sum, SPIMD, or the MPBMD did not lead to improvements. The distances of one event from beam A to all events from beam B are calculated and their inverses are averaged. This process is repeated for each individual event so that each event is assigned its own similarity factor. A certain fraction of the events with the highest similarity factor per beam was selected, and for those events, the distance calculation and event selection process were repeated in an iterative manner until a termination criterion is reached. The number of iterations was configurable. The termination criterion describes the number of events at which the process was stopped. Due to the exponential intensity decrease depending on the beam depth, this criterion was based on the Lambert–Beer law [62] and calculated independently for both beams.

The number of events that act as a threshold to terminate the iteration process ($\#\gamma_t$) was calculated from the number of events in a configurable range, given by d_1 and d_2, around the intersection point

$$\#\gamma_t = \#\gamma_0 \cdot \left(e^{-\mu \cdot d_1} - e^{-\mu \cdot d_2}\right). \tag{5}$$

The initial number of events ($\#\gamma_0$) was calculated theoretically according to the Lambert–Beer law from the number of detected events ($\#\gamma_d$) and the beam path length within the scintillator (d_p)

$$\#\gamma_0 = \#\gamma_d \cdot \left(1 - e^{-\mu \cdot d_p}\right) \tag{6}$$

with μ as the attenuation coefficient for the used LYSO scintillator ($\mu = 0.087\ \text{mm}^{-1}$). In this work, 20 iterations were chosen for reasons of algorithm stability, although five iterations already achieved similar results.

Using the planar position from the previous planar-monolithic calibration, the events in question can be constrained around a range around the intersection point (planar range) already at the beginning of the routine. This can mitigate a bias effect that pulls the intersection clusters toward upper DOI positions due to the increased gamma interaction density there. In this evaluation, the planar range was set to ± 2 mm to be wider than the planar-monolithic SR of 2.3 mm.

Due to the described individual operation of the DPCs, missing DPC readouts and thus missing optical photon counts in the events occur at about 25% in the measurements performed. Since the dual-angle method would sort out more of these events, an imputation is performed temporarily for the routine. The missing DPC photon counts are supplemented by the mean of the photon counts of similar events via the k-Nearest Neighbors Imputer [60] with two neighbors.

In principle, the dual-angle method can also be applied to a measurement with two different fan-beam irradiation angles. However, no performance improvement can be expected when replacing one of the angular irradiations with steeper irradiation. Therefore, both angles should be chosen for in-system calibration in such a way that a reasonable tradeoff between performance and mechanical realization is given.

G. Energy Calibration

For part of the evaluations, an energy filter of (435 to 585) keV was applied to the test dataset. To the training dataset only the photon filter from the preprocessing was applied for all evaluations. The energy determination required for this is based on the energy calibration described in [31]. The photopeak of the events was assigned the energy of 511 keV. The basis for this is the sum of photon counts of the DPC column under the slab containing the main DPC of each event. For a more specific calibration, the

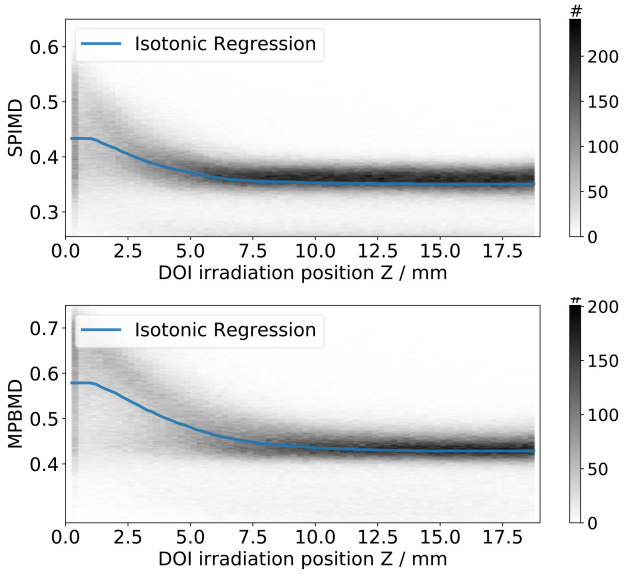

Fig. 4. Single input feature (SPIMD and MPBMD) versus reference DOI irradiation position of the events. An IR (blue) was applied.

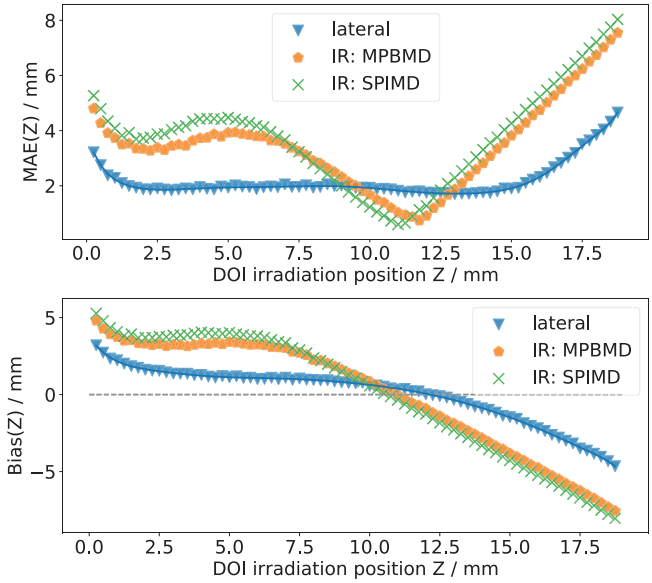

Fig. 5. MAE and bias course plot for the individual DOI irradiation positions comparing the lateral irradiation and IR methods. Both IR methods show a noticeable bias effect toward mid-upper DOI positions.

photopeak assignment was performed separately for 8×8 voxels in the planar plane after planar position estimation, to compensate for different detector responses over the detector volume with an additional subdivision of voxels to main DPCs occurring in this voxel. Events with a missing DPC readout were interpolated via a mean light distribution, leading overall to an energy resolution of 14%. An additional voxelization in DOI would improve the energy resolution but was not performed at this point to avoid dependence of the DOI positioning algorithms.

IV. Results

A. Lateral Irradiation Method

The proven lateral irradiation serves as a positioning benchmark for the angular calibration methods. An MAE of 2.17 mm and an SR of 3.5 mm were achieved. Applying an energy filter of (435 to 585) keV to the test dataset, both MAE and SR improve to 1.80 and 3.1 mm, respectively.

B. Single Input Feature-Based Method

For slabs, the parameters SPIMD and MPIBMD showed no DOI dependence for mid to upper DOI positions (see Fig. 4). This was reflected in a strongly deteriorated positioning performance compared to the lateral irradiation-based methods. An MAE of 3.5 and 3.2 mm for the features SPIMD and MPBMD, respectively, resulted. A pronounced bias effect toward $Z \sim 12$ mm is visible (Fig. 5), roughly corresponding to the center of the constant range of the feature in Fig. 4.

C. Mono-Angle Method

The mono-angle routine showed improving MAE distributions for shallower irradiation angles (Fig. 6). This is also reflected in the bias vector, with flatter distributions toward the crystal surfaces. The stronger bias effect for steeper irradiation angles leads to a better MAE in central DOI regions while strongly decreasing the MAE performance

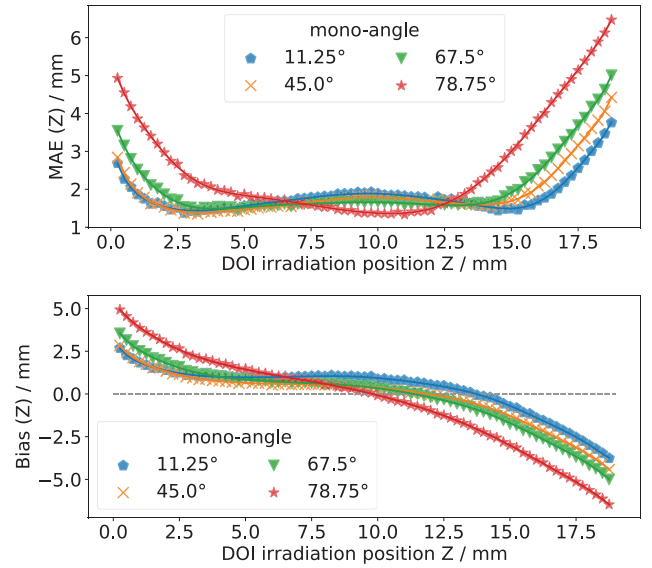

Fig. 6. Mono-angle method. Positioning performance comparison of the MAE and bias parameter between different irradiation angles. An energy filter of (435 to 585) keV was applied to the test dataset.

toward the crystal edges. Thus, the MAE overall decreases with increasing irradiation angles as seen in Fig. 10.

Comparing the mono-angle method at an angle of 45° to the lateral irradiation method with an applied energy filter of (435 to 585) keV to the test dataset (Fig. 7), a slightly more pronounced bias effect is visible that overall tends to lower DOI positions with a ∼6% decreased MAE and ∼5% decreased SR performance (Table I). Without the energy filter, the MAE decreases to ∼7%, while the SR is in the range of ∼3% to the lateral irradiation method.

D. Dual-Angle Method

The dual-angle routine showed an improved MAE curve for shallower beam angles (Fig. 8). Likewise,

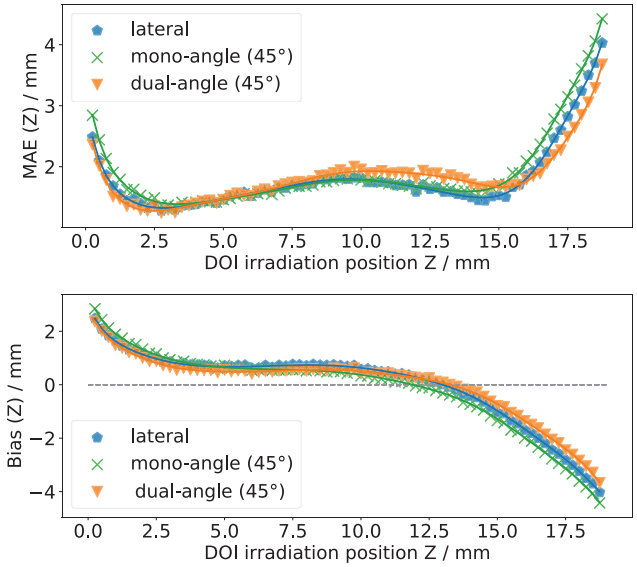

Fig. 7. MAE and bias positioning performance comparison between the lateral method and both the angular irradiation-based methods at an irradiation angle of $\alpha = 45°$. An energy filter of (435 to 585) keV was applied to the test datasets.

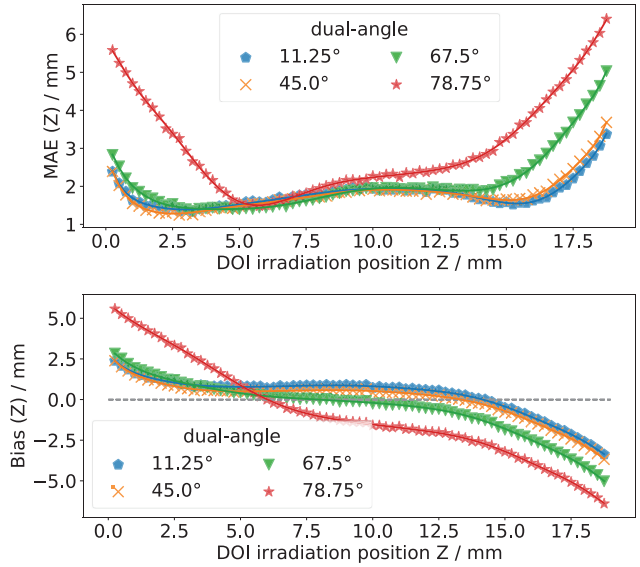

Fig. 8. Dual-angle method. Positioning performance comparison of the MAE and Bias parameter between different irradiation angles at a planar range of ±2 mm. An energy filter of (435 to 585) keV was applied to the test dataset.

TABLE I
PERFORMANCE PARAMETER COMPARISON BETWEEN THE DOI CALIBRATION METHODS AT AN IRRADIATION ANGLE OF $\alpha = 45°$ FOR THE ANGULAR IRRADIATION-BASED METHODS. RESULTS ARE SHOWN WITHOUT A SPECIFIC ENERGY FILTER, AND WITH AN ENERGY FILTER OF (435 TO 585) KEV APPLIED TO THE TEST DATASET

$\alpha = 45°$	*lateral*	*mono-angle*	*dual-angle*
	only photon filter / *energy filter* (435 to 585) keV		
MAE [mm]	2.17 / 1.80	2.32 /1.90	2.27 / 1.81
SR [mm]	3.52 /3.06	3.64 / 3.20	3.56 / 3.13
r_{50} **[mm]**	1.59 / 1.32	1.74 / 1.43	1.57 / 1.28
r_{90} **[mm]**	4.84 / 3.84	5.06 / 3.96	5.22 / 3.90

the bias curve flattens out, similar to the mono-angle method. The algorithm deteriorates noticeably at the irradiation angle of 78.75° for lower DOI positions.

At an incidence angle of 45°, the routine came close to the lateral irradiation method by ∼5% MAE and ∼3% SR (see Table I). Using the energy filter on the test dataset, the dual-angle method at the 45° angle scored with deviations of <1% MAE, and ∼2% SR compared to the lateral method. The PSFs in Fig. 9 show a slight bias toward lower DOI positions and compared to the mono-angle method a slimmer distribution at the r_{50} while performing comparable at the r_{90}. Fig. 10 shows the trend of improving MAE performance for more shallow irradiation angles. The energy filter leads to a slightly stronger improvement of the dual-angle method at mid to shallow irradiation angles compared to the mono-angle method.

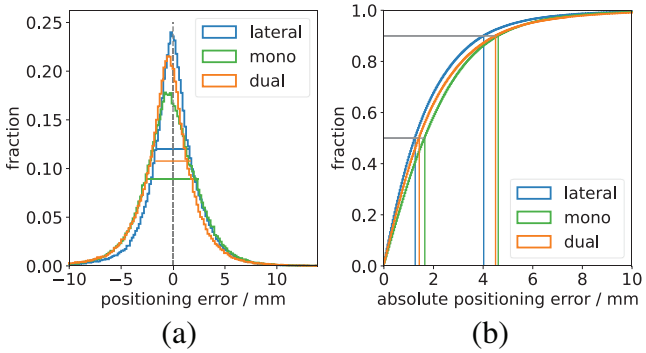

Fig. 9. Normed PSFs for the angular and lateral irradiation methods at $\alpha = 45°$ and an energy filter of (435 to 585) keV. (a) Positioning error distribution with the FWHM represented by the horizontal lines. (b) Cumulative positioning error distribution with the vertical lines representing the r_{50} and r_{90}.

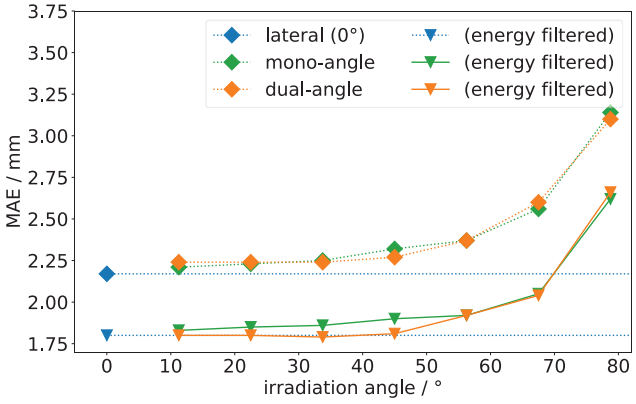

Fig. 10. MAE positioning performance comparison for different irradiation angles of the angular irradiation-based methods. The lateral irradiation method is plotted at $\alpha = 0°$ and from there as a dashed line for reference.

The energy spectrum of the dual-angle training dataset reveals a more pronounced photopeak area and a suppressed Compton region compared to the lateral and mono-angle datasets Fig. 11.

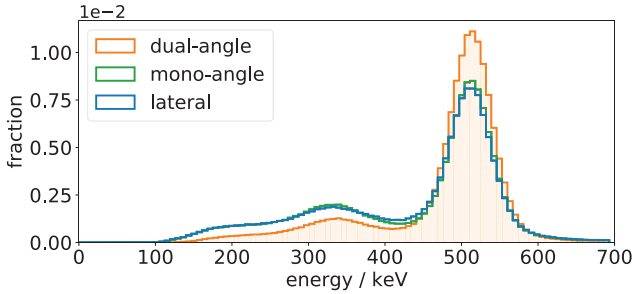

Fig. 11. Normed energy spectra of the angular irradiation-based training datasets ($\alpha = 45°$) and the lateral irradiation training dataset. The dual-angle energy spectrum (orange) shows a more pronounced 511-keV energy peak with a suppressed Compton spectrum.

V. Discussion

In this work, we have compared four different DOI calibration methods. We introduced and demonstrated the functionality of two methods based on angular detector irradiation toward DOI in-system calibration.

The introduced DOI calibration routines based on angular detector irradiation (mono-angle, dual-angle) achieved positioning performances very close to the proven lateral irradiation method for beam angles shallower than 60° and the used slab detectors. Conceptually, both routines are transferable to different digitalization and readout techniques that output light patterns, both individual read-out channels as well as multiplexing schemes. This additionally applies to different light-sharing scintillator geometries. The approach based on single input features, on the other hand, did not show a pronounced DOI dependence of the investigated features resulting in a noncompetitive DOI positioning performance. In the current state, already published single observables did not reveal a good mapping with the DOI position as well, in contrast to monolithic scintillators, presumably due to a higher number of reflections of optical photons and more compressed light patterns. DOI-dependent parameters for slabs in the upper DOI positions, however, would also be a supplement for the angular calibration methods so that further investigation will be done in future work.

Both angular irradiation-based methods achieve better MAE positioning performance for shallower beam angles that approach the lateral irradiation method (Fig. 10). This is to be expected since the calculated reference DOI position by the angular irradiation methods would match the lateral irradiation at $\alpha = 0°$.

For steeper irradiation angles toward $\alpha = 90°$, both angular irradiation-based routines decrease in positioning performance. The reason for this in the dual-angle method is in particular the widening of the intersection area in DOI direction within the planar range. This mainly degrades the upper DOI positions (Fig. 8), probably due to the smaller differences between the light distributions as seen in the single input feature-based method. For 78.75° the algorithm decreases noticeably at low DOI positions also due to the intersection cluster widening and the higher event density at upper positions due to the exponential gamma beam intensity decay in the scintillator volume. For the mono-angle method, the increasing influence of the planar positioning uncertainty for steeper incidence angles significantly affects the positioning performance. While the planar SR of 2.3 mm theoretically propagates into a DOI deviation of 0.4 mm at 11.25°, it increases to a deviation of 2.3 mm at 45°. Since the mono-angle algorithm rejects events that would be assigned a DOI outside the detector volume, events are increasingly discarded near the edges in the DOI direction. This results in an amplifying bias effect toward the detector center (Fig. 6).

Without energy filters, both angular irradiation-based methods perform similarly at the different irradiation angles. With an energy filter of (435 to 585) keV applied to the test dataset, both angular irradiation methods improve in MAE by about 20% for all angles, similar to the lateral irradiation method. In particular, the dual-angle method surpasses the mono-angle method especially at more shallow irradiation angles and performs equivalently to the lateral irradiation method up to an angle of 45°. This could be due to the more confined dual-angle training dataset. The dual-angle routine aims for the most similar events in an intersection cluster so that events of lower probability are more likely filtered. This is shown in Fig. 11 with a higher fraction of events in the 511-keV vicinity compared to the other methods, and thus, a higher fraction of events in the selected energy window for the test dataset. The relative improvement of the r_{90} value to the lateral irradiation method with energy filter and the overall good r_{50} performance at 45° (Table I) further underlines this assumption.

The PSFs in Fig. 9 reveal a higher peak fraction for the lateral irradiation method compared to the angular routines. Comparing Fig. 9(a) with Fig. 9(b) shows an increasing peak fraction especially for the mono-angle routine when excluding the edge DOI positions closer than 3 mm to the crystal surfaces.

One difference between a PET system and our test setup is that the detectors in the system have neighboring detectors that can attenuate the gamma beam intensity and widen the beam by scatter. This especially affects the detector edges, which could be freely irradiated in our test setup, as long as the beam is not radiated through the crystal itself. However, we have investigated the planar dependence of the DOI performance, and the calibration methods showed no significant difference on the used test dataset. Therefore, we assume that the results from the test setup can be achieved at the system level. The detectors on the axial ends of the scanner, however, could be irradiated directly with higher statistics or a shorter duration assuming no shielding end plate or septa in the scanner. In PET systems with end plates, the mono-angle method would remain conceptually unaffected, while the dual-angle method would encounter difficulties.

For feasible in-system calibration, not only the positioning performance must be considered, but also the mechanical realization, setup cost, as well as computational efforts. The mono-angle method is less susceptible to mechanical inaccuracies in a possible collimator setup, compared to the dual-angle method, and is less complex, also in terms of required processing. Conceptually feasible are the angular methods of irradiation angles around 30° and steeper depending on the ring diameter and the axial field-of-view. As a tradeoff between performance and applicability, the mono-angle method might be best suitable at an angle of incidence of (30 to 55)°. With enhanced planar position estimation, the mono-angle routine

in particular can be further improved. Irradiation along the planar-segmented direction for high-resolution slab designs would also be conceivable.

The fixation and precise alignment of the collimator in the PET system also plays a central role in mechanical realization. A 3-D translation stage/robot could move the collimator into positions according to the concepts in Fig. 1. This would be simplified by a lighter and smaller collimator than the one used in our test setup. A corresponding adjustment is reasonably possible according to Monte Carlo simulations conducted with GATE in which the beam profiles for different fan-beam collimator lengths were investigated. The singles spectra of 511-keV photons showed that for one-half of the collimator length used in the presented experiments the FWHM of the beam profile is within 8% and the full-width at tenth maximum (FWTM) within 15%. The exact mechanical realization relies on the targeted PET system and stays open for future work as the present paper presented the general concept.

VI. Conclusion

We designed two DOI calibration methods for (semi-)monolithic detectors based on angular detector irradiation with a fan-beam collimator and a GTB-based gamma position estimation. The methods were experimentally evaluated in terms of their positioning performance depending on the angle of incidence. The achieved positioning performance of the mono-angle and dual-angle methods came close to the known lateral irradiation method. Especially the dual-angle routine performed equivalently for angles below 45° and an energy filter of (435 to 585) keV applied to the test dataset. The mono-angle method got close to 5% MAE up to angles of about 45° making both methods a good pathway toward in-system calibration. Comparing mono-angle and dual-angle methods, the mono-angle method is simpler in application and implementation, while the dual-angle method provides an overall slightly better DOI positioning. Conceptually, both routines can also be used for irradiation in the planar-segmented slab direction, where especially the mono-angle method could benefit here from highly segmented slab designs. Corresponding experiments including in-system calibration are planned with a focus on mono-angle method implementation.

Acknowledgment

The authors thank the scientific workshop of the RWTH University Hospital Aachen for manufacturing the technical components.

All authors declare that they have no known conflicts of interest in terms of competing financial interests or personal relationships that could have an influence or are relevant to the work reported in this article.

References

[1] S. S. Anand, H. Singh, and A. K. Dash, "Clinical applications of PET and PET-CT," *Med. J. Armed Forces India*, vol. 65, no. 4, pp. 353–358, 2009, doi: 10.1016/S0377-1237(09)80099-3.

[2] N. L. Albert et al., "Response assessment in neuro-oncology working group and European association for neuro-oncology recommendations for the clinical use of PET imaging in gliomas," *Neuro Oncol.*, vol. 18, no. 9, pp. 1199–1208, 2016, doi: 10.1093/neuonc/now058.

[3] R.-C. Lu et al., "Positron-emission tomography for hepatocellular carcinoma: Current status and future prospects," *World J. Gastroenterol.*, vol. 25, no. 32, pp. 4682–4695, 2019, doi: 10.3748/wjg.v25.i32.4682.

[4] J. L. Humm, A. Rosenfeld, and A. del Guerra, "From PET detectors to PET scanners," *Eur. J. Nucl. Med. Mol. Imag.*, vol. 30, no. 11, pp. 1574–1597, 2003, doi: 10.1007/s00259-003-1266-2.

[5] S. Vandenberghe, P. Moskal, and J. S. Karp, "State of the art in total body PET," *EJNMMI Phys.*, vol. 7, no. 1, p. 35, Dec. 2020, doi: 10.1186/s40658-020-00290-2.

[6] B. A. Spencer et al., "Performance evaluation of the uEXPLORER total-body PET/CT scanner based on NEMA NU 2-2018 with additional tests to characterize PET scanners with a long axial field of view," *J. Nucl. Med.*, vol. 62, no. 6, pp. 861–870, Jun. 2021, doi: 10.2967/jnumed.120.250597.

[7] J. van Sluis et al., "Performance characteristics of the digital biograph vision PET/CT system," *J. Nucl. Med.*, vol. 60, no. 7, pp. 1031–1036, 2019, doi: 10.2967/jnumed.118.215418.

[8] Y. Lai et al., "H^2RSPET: A 0.5 mm resolution high-sensitivity small-animal PET scanner, a simulation study," *Phys. Med. Biol.*, vol. 66, no. 6, 2021, Art. no. 65016, doi: 10.1088/1361-6560/abe558.

[9] T. Yamaya, "PET imaging innovation by DOI detectors," in *Perspectives on Nuclear Medicine for Molecular Diagnosis and Integrated Therapy*. Tokyo, Japan: Springer, 2016, pp. 39–49, doi: 10.1007/978-4-431-55894-1_3.

[10] J. P. Schmall, J. S. Karp, M. Werner, and S. Surti, "Parallax error in long-axial field-of-view PET scanners—A simulation study," *Phys. Med. Biol.*, vol. 61, no. 14, pp. 5443–5455, 2016, doi: 10.1088/0031-9155/61/14/5443.

[11] I. Mohammadi, I. F. C. Castro, P. M. M. Correia, A. L. M. Silva, and J. F. C. A. Veloso, "Minimization of parallax error in positron emission tomography using depth of interaction capable detectors: Methods and apparatus," *Biomed. Phys. Eng. Exp.*, vol. 5, no. 6, Oct. 2019, Art. no. 62001, doi: 10.1088/2057-1976/AB4A1B.

[12] T. Tsuda et al., "A four-layer depth of interaction detector block for small animal PET," *IEEE Trans. Nucl. Sci.*, vol. 51, no. 5, pp. 2537–2542, Oct. 2004, doi: 10.1109/TNS.2004.835739.

[13] H. G. Kang, G. B. Ko, J. T. Rhee, K. M. Kim, J. S. Lee, and S. J. Hong, "A dual-ended readout detector using a meantime method for SiPM TOF-DOI PET," *IEEE Trans. Nucl. Sci.*, vol. 62, no. 5, pp. 1935–1943, Oct. 2015, doi: 10.1109/TNS.2015.2449891.

[14] A. Kishimoto et al., "Development of a dual-sided readout DOI-PET module using large-area monolithic MPPC-arrays," *IEEE Trans. Nucl. Sci.*, vol. 60, no. 1, pp. 38–43, Feb. 2013, doi: 10.1109/TNS.2012.2233215.

[15] V. Tabacchini, S. Surti, G. Borghi, J. S. Karp, and D. R. Schaart, "Improved image quality using monolithic scintillator detectors with dual-sided readout in a whole-body TOF-PET ring: A simulation study," *Phys. Med. Biol.*, vol. 62, no. 5, p. 2018, Feb. 2017, doi: 10.1088/1361-6560/AA56E1.

[16] M. Morrocchi et al., "Depth of interaction determination in monolithic scintillator with double side SiPM readout," *EJNMMI Phys.*, vol. 4, no. 1, pp. 1–25, Dec. 2017, doi: 10.1186/s40658-017-0180-9.

[17] G. Borghi, B. J. Peet, V. Tabacchini, and D. R. Schaart, "A 32 mm × 32 mm × 22 mm monolithic LYSO:Ce detector with dual-sided digital photon counter readout for ultrahigh-performance TOF-PET and TOF-PET/MRI," *Inst. Phys. Eng. Med. Phys. Med. Biol.*, vol. 61, no. 13, pp. 4929–4949, 2016, doi: 10.1088/0031-9155/61/13/4929.

[18] T. K. Lewellen, M. Janes, and R. S. Miyaoka, "DMice-a depth-of-interaction detector design for PET scanners," in *Proc. IEEE Nucl. Sci. Symp. Conf. Rec.*, vol. 4, 2004, pp. 2388–2392, doi: 10.1109/NSSMIC.2004.1462737.

[19] A. LaBella et al., "High-resolution depth-encoding PET detector module with prismatoid light-guide array," *J. Nucl. Med.*, vol. 61, no. 10, pp. 1528–1533, Oct. 2020, doi: 10.2967/JNUMED.119.239343.

[20] M. Schmand, L. Eriksson, M. E. Casey, K. Wienhard, G. Flügge, and R. Nutt, "Advantages using pulse shape discrimination to assign the depth of interaction information (DOI) from a multi layer phoswich detector," *IEEE Trans. Nucl. Sci.*, vol. 46, no. 4, pp. 985–990, Aug. 1999, doi: 10.1109/23.790808.

[21] H. Uchida, T. Sakai, H. Yamauchi, K. Hakamata, K. Shimizu, and T. Yamashita, "A novel single-ended readout depth-of-interaction PET detector fabricated using sub-surface laser engraving," *Phys. Med. Biol.*, vol. 61, no. 18, p. 6635, Aug. 2016, doi: 10.1088/0031-9155/61/18/6635.

[22] R. Marcinkowski, P. Mollet, R. van Holen, and S. Vandenberghe, "Sub-millimetre DOI detector based on monolithic LYSO and digital SiPM for a dedicated small-animal PET system," *Phys. Med. Biol.*, vol. 61, no. 5, p. 2196, Feb. 2016, doi: 10.1088/0031-9155/61/5/2196.

[23] P. Bruyndonckx et al., "Evaluation of machine learning algorithms for localization of photons in undivided scintillator blocks for PET detectors," *IEEE Trans. Nucl. Sci.*, vol. 55, no. 3, pp. 918–924, Jun. 2008, doi: 10.1109/TNS.2008.922811.

[24] G. Borghi, V. Tabacchini, and D. R. Schaart, "Towards monolithic scintillator based TOF-PET systems: Practical methods for detector calibration and operation," *Phys. Med. Biol.*, vol. 61, no. 13, p. 4904, Jun. 2016, doi: 10.1088/0031-9155/61/13/4904.

[25] F. Mueller, D. Schug, P. Hallen, J. Grahe, and V. Schulz, "Gradient tree boosting-based positioning method for monolithic scintillator crystals in positron emission tomography," *IEEE Trans. Radiat. Plasma Med. Sci.*, vol. 2, no. 5, pp. 411–421, Sep. 2018, doi: 10.1109/TRPMS.2018.2837738.

[26] F. Muller, D. Schug, P. Hallen, J. Grahe, and V. Schulz, "A novel DOI positioning algorithm for monolithic scintillator crystals in PET based on gradient tree boosting," *IEEE Trans. Radiat. Plasma Med. Sci.*, vol. 3, no. 4, pp. 465–474, Jul. 2019, doi: 10.1109/trpms.2018.2884320.

[27] A. Gonzalez-Montoro et al., "Evolution of PET detectors and event positioning algorithms using monolithic scintillation crystals," *IEEE Trans. Radiat. Plasma Med. Sci.*, vol. 5, no. 3, pp. 282–305, May 2021, doi: 10.1109/TRPMS.2021.3059181.

[28] S. Seifert et al., "Monolithic $LaBr_3$:Ce crystals on silicon photomultiplier arrays for time-of-flight positron emission tomography," *Phys. Med. Biol.*, vol. 57, no. 8, pp. 2219–2233, Apr. 2012, doi: 10.1088/0031-9155/57/8/2219.

[29] J. Barrio et al., "PET detector based on a semi-monolithic crystal with DOI and TOF capabilities," in *Proc. IEEE Nucl. Sci. Symp. Med. Imag. Conf. (NSS/MIC)*, Aug. 2021, pp. 1–3, doi: 10.1109/nss/mic42677.2020.9508047.

[30] F. Mueller, D. Schug, M. Hammerath, C. Gorjaew, T. Solf, and V. Schulz, "Machine learning-based calibration of (semi-)monolithic detectors enabling depth of interaction-encoding and time-of-flight capabilities in clinical PET systems," *NuklearMedicine*, vol. 59, no. 2, p. 99, 2020, doi: 10.1055/s-0040-1708150.

[31] F. Mueller, S. Naunheim, Y. Kuhl, D. Schug, T. Solf, and V. Schulz, "A semi-monolithic detector providing intrinsic DOI-encoding and sub-200 ps CRT TOF-capabilities for clinical PET applications," *Med. Phys.*, vol. 49, no. 12, pp. 7469–7488, Nov. 2022, doi: 10.1002/MP.16015.

[32] D. Schug et al., "Data processing for a high resolution preclinical PET detector based on philips DPC digital SiPMs," *IEEE Trans. Nucl. Sci.*, vol. 62, no. 3, pp. 669–678, Jun. 2015, doi: 10.1109/TNS.2015.2420578.

[33] Z. Li, M. Wedrowski, P. Bruyndonckx, and G. Vandersteen, "Nonlinear least-squares modeling of 3D interaction position in a monolithic scintillator block," *Phys. Med. Biol.*, vol. 55, no. 21, pp. 6515–6532, Nov. 2010, doi: 10.1088/0031-9155/55/21/012.

[34] T. Ling, T. H. Burnett, T. K. Lewellen, and R. S. Miyaoka, "Parametric positioning of a continuous crystal PET detector with depth of interaction decoding," *Phys. Med. Biol.*, vol. 53, no. 7, pp. 1843–1863, Apr. 2008, doi: 10.1088/0031-9155/53/7/003.

[35] S. Bae and J. S. Lee, "Wasserstein distance-based nonlinear dimensionality reduction for depth-of-interaction decoding in monolithic crystal PET detector," *J. Nucl. Med.*, vol. 63, no. s2, p. 3318, 2022.

[36] G. Borghi, V. Tabacchini, S. Seifert, and D. R. Schaart, "Experimental validation of an efficient fan-beam calibration procedure for *k*-nearest neighbor position estimation in monolithic scintillator detectors," *IEEE Trans. Nucl. Sci.*, vol. 62, no. 1, pp. 57–67, Feb. 2015, doi: 10.1109/TNS.2014.2375557.

[37] N. Gross-Weege, D. Schug, P. Hallen, and V. Schulz, "Maximum likelihood positioning algorithm for high-resolution PET scanners," *Med. Phys.*, vol. 43, no. 6, pp. 3049–3061, Jun. 2016, doi: 10.1118/1.4950719.

[38] Y. Wang, Y. Xiao, X. Cheng, D. Li, and L. Wang, "An FPGA-based real-time maximum likelihood 3D position estimation for a continuous crystal PET detector," *IEEE Trans. Nucl. Sci.*, vol. 63, no. 1, pp. 37–43, Feb. 2016, doi: 10.1109/TNS.2015.2506739.

[39] A. Iborra, A. J. González, A. González-Montoro, A. Bousse, and D. Visvikis, "Ensemble of neural networks for 3D position estimation in monolithic PET detectors," *Phys. Med. Biol.*, vol. 64, no. 19, Oct. 2019, Art. no. 195010, doi: 10.1088/1361-6560/ab3b86.

[40] M. Freire, A. Gonzalez-Montoro, F. Sanchez, J. M. Benlloch, and A. J. Gonzalez, "Calibration of gamma ray impacts in monolithic-based detectors using Voronoi diagrams," *IEEE Trans. Radiat. Plasma Med. Sci.*, vol. 4, no. 3, pp. 350–360, May 2020, doi: 10.1109/trpms.2019.2947716.

[41] C. Ritzer, P. Hallen, D. Schug, and V. Schulz, "Intercrystal scatter rejection for pixelated PET detectors," *IEEE Trans. Radiat. Plasma Med. Sci.*, vol. 1, no. 2, pp. 191–200, Mar. 2017, doi: 10.1109/tns.2017.2664921.

[42] M. Freire, G. Cañizares, S. Echegoyen, A. Gonzalez-Montoro, and A. J. Gonzalez, "Reducing calibration time in PET systems based on monolithic crystals," *Front. Med.*, vol. 8, p. 2095, Nov. 2021, doi: 10.3389/fmed.2021.734476.

[43] R. Hetzel, F. Mueller, J. Grahe, A. Honné, D. Schug, and V. Schulz, "Characterization and simulation of an adaptable fan-beam collimator for fast calibration of radiation detectors for PET," *IEEE Trans. Radiat. Plasma Med. Sci.*, vol. 4, no. 5, pp. 538–545, Sep. 2020, doi: 10.1109/trpms.2020.2990651.

[44] Y. Kuhl, S. Naunheim, F. Müller, D. Schug, and V. Schulz, "Design and experimental characterization of a multi fan beam collimator for fast calibration of (semi-)monolithic scintillators," in *Proc. IEEE NSS/MIC*, vol. 2, Sep. 2021.

[45] T. Dey, D. Schug, P. Hallen, V. Schulz, and F. Mueller, "Vorrichtung zur Kalibrierung eines PET-systems," Patent DE102 019 215 437 A1, 2019. Accessed: Mar. 10, 2023. [Online]. Available: https://patents.google.com/patent/DE102019215437A1/de?q=%%BCller+schug+schulz+dey)&oq%%BCller+schug+schulz+dey

[46] M. Freire et al., "Experimental validation of a rodent PET scanner prototype based on a single LYSO crystal tube," *IEEE Trans. Radiat. Plasma Med. Sci.*, vol. 6, no. 6, pp. 697–706, Jul. 2022, doi: 10.1109/TRPMS.2021.3124448.

[47] Y. Wang, W. Zhu, X. Cheng, and D. Li, "3D position estimation using an artificial neural network for a continuous scintillator PET detector," *Phys. Med. Biol.*, vol. 58, no. 5, pp. 1375–1390, 2013, doi: 10.1088/0031-9155/58/5/1375.

[48] Z. Li, *Study of 3D Position Determination of the Interaction Point in Monolithic Scintillator Blocks for PET*, Vrije Universiteit Brussel, Brussel, Belgium, 2011.

[49] X. Li and L. R. Furenlid, "Fast monolithic detector calibration method—A simulation study," in *Proc. IEEE Nucl. Sci. Symp. Med. Imag. Conf. (NSS/MIC)*, 2018, pp. 1–7.

[50] X. Li, L. Tao, C. S. Levin, and L. R. Furenlid, "Virtual point source synthesis method for 3D scintillation detector characterization," Jun. 2021, *arXiv:2106.12219*.

[51] D. Schug, F. Kiessling, and V. Schulz, "Fast and unbiased 3D calibration method of arbitrary scintillator based PET detectors," in *Proc. IEEE Nucl. Sci. Symp. Conf. Rec.*, 2013, pp. 1–4, doi: 10.1109/NSSMIC.2013.6829084.

[52] "Tile-TEK user manual." 2016. [Online]. Available: http://www.digitalphotoncounting.comhttp://www.digitalphotoncounting.com

[53] T. Frach, G. Prescher, C. Degenhardt, R. de Gruyter, A. Schmitz, and R. Ballizany, "The digital silicon photomultiplier—Principle of operation and intrinsic detector performance," in *Proc. IEEE Nucl. Sci. Symp. Conf. Rec.*, 2009, pp. 1959–1965, doi: 10.1109/NSSMIC.2009.5402143.

[54] V. Tabacchini, V. Westerwoudt, G. Borghi, S. Seifert, and D. R. Schaart, "Probabilities of triggering and validation in a digital silicon photomultiplier," *J. Instrum.*, vol. 9, Jun. 2014, Art. no. P06016, doi: 10.1088/1748-0221/9/06/P06016.

[55] C. Wassermann et al., "High throughput software-based gradient tree boosting positioning for PET systems," *Biomed. Phys. Eng. Exp.*, vol. 7, no. 5, 2021, Art. no. 55023, doi: 10.1088/2057-1976/ac11c0.

[56] K. Krueger, F. Mueller, P. Gebhardt, B. Weissler, D. Schug, and V. Schulz, "High-throughput FPGA-based inference of gradient tree boosting models for position estimation in PET detectors," *IEEE Trans. Radiat. Plasma Med. Sci.*, vol. 7, no. 3, pp. 253–262, Mar. 2023, doi: 10.1109/TRPMS.2023.3238904.

[57] (Nat. Electr. Manuf. Assoc. (NEMA), Rosslyn, VA, USA). *NEMA NU4-2008: Performance Measurements of Small Animal Positron Emission Tomographs*. (2008). [Online]. Available: www.nema.org

[58] H. T. van Dam et al., "A practical method for depth of interaction determination in monolithic scintillator PET detectors," *Phys. Med. Biol.*, vol. 56, no. 13, pp. 4135–4145, Jul. 2011, doi: 10.1088/0031-9155/56/13/025.

[59] A. González-Montoro et al., "Performance study of a large monolithic LYSO PET detector with accurate photon DOI using retroreflector layers," *IEEE Trans. Radiat. Plasma Med. Sci.*, vol. 1, no. 3, pp. 229–237, May 2017, doi: 10.1109/trpms.2017.2692819.

[60] F. Pedregosa et al. "Scikit-learn: Machine learning in python." 2011. [Online]. Available: http://scikit-learn.sourceforge.net

[61] D. Habs, M. M. Günther, M. Jentschel, and W. Urban, "Refractive index of silicon at γ ray energies," *Phys. Rev. Lett.*, vol. 108, May 2012, Art. no. 184802, doi: 10.1103/PhysRevLett.108.184802.

[62] D. F. Swineharf, "The Beer-Lambert law," *J. Chem. Educ.*, vol. 39, no. 7, pp. 333–335, 1962, doi: 10.1021/ED039P333.